Effect of porosity of a functionally-graded scaffold for the treatment of corticosteroid-associated osteonecrosis of the femoral head in rabbits

Masahiro Maruyama [a,1], Chi-Chun Pan [a,d,1], Seyedsina Moeinzadeh [a], Hunter W. Storaci [a], Roberto Alfonso Guzman [a], Elaine Lui [a,d], Masaya Ueno [a], Takeshi Utsunomiya [a], Ning Zhang [a], Claire Rhee [a], Zhenyu Yao [a], Michiaki Takagi [e], Stuart B. Goodman [a,c,*], Yunzhi Peter Yang [a,b,c,**]

[a] Department of Orthopaedic Surgery, Stanford University School of Medicine, Stanford, CA, USA
[b] Material Science and Engineering, Stanford University School of Medicine, Stanford, CA, USA
[c] Bioengineering, Stanford University School of Medicine, Stanford, CA, USA
[d] Department of Mechanical Engineering, Stanford University School of Engineering, Stanford, CA, USA
[e] Department of Orthopaedic Surgery, Yamagata University Faculty of Medicine, Yamagata, Japan

ARTICLE INFO

ABSTRACT

Background/Objective: Core decompression (CD) with scaffold and cell-based therapies is a promising strategy for providing both mechanical support and regeneration of the osteonecrotic area for early stage osteonecrosis of the femoral head (ONFH). We designed a new 3D printed porous functionally-graded scaffold (FGS) with a central channel to facilitate delivery of transplanted cells in a hydrogel to the osteonecrotic area. However, the optimal porous structural design for the FGS for the engineering of bone in ONFH has not been elucidated. The aim of this study was to fabricate and evaluate two different porous structures (30% or 60% porosity) of the FGSs in corticosteroid-associated ONFH in rabbits.

Methods: Two different FGSs with 30% or 60% porosity containing a 1-mm central channel were 3D printed using polycaprolactone and β-tricalcium phosphate. The FGS was 3-mm diameter and 32-mm length and was composed of three segments: 1-mm in length for the non-porous proximal segment, 22-mm in length for the porous (30% versus 60%) middle segment, and 9-mm in length for the 15% porous distal segment. Eighteen male New Zealand White rabbits were given a single dose of 20 mg/kg methylprednisolone acetate intramuscularly. Four weeks later, rabbits were divided into three groups: the CD group, the 30% porosity FGS group, and the 60% porosity FGS group. In the CD group, a 3-mm diameter drill hole was created into the left femoral head. In the FGS groups, a 30% or 60% porosity implant was inserted into the bone tunnel. Eight weeks postoperatively, femurs were harvested and microCT, mechanical, and histological analyses were performed.

Results: The actual porosity and pore size of the middle segments were $26.4\% \pm 2.3\%$ and 699 ± 56 μm in the 30% porosity FGS, and $56.0\% \pm 4.5\%$ and 999 ± 71 μm in the 60% porosity FGS, respectively using microCT analysis. Bone ingrowth ratio in the 30% porosity FGS group was $73.9\% \pm 15.8\%$, which was significantly higher than $39.5\% \pm 13.0\%$ in the CD group on microCT ($p < 0.05$). Bone ingrowth ratio in the 60% porosity FGS group ($61.3\% \pm 30.1\%$) showed no significant differences compared to the other two groups. The stiffness at the bone tunnel site in the 30% porosity FGS group was 582.4 ± 192.3 N/mm^3, which was significantly higher than 338.7 ± 164.6 N/mm^3 in the 60% porosity FGS group during push-out testing ($p < 0.05$). Hematoxylin and eosin staining exhibited thick and mature trabecular bone around the porous FGS in the 30% porosity FGS group, whereas thinner, more immature trabecular bone was seen around the porous FGS in the 60% porosity FGS group.

Conclusion: These findings indicate that the 30% porosity FGS may enhance bone regeneration and have superior biomechanical properties in the bone tunnel after CD in ONFH, compared to the 60% porosity FGS.

Translation potential statement: The translational potential of this article: This FGS implant holds promise for improving outcomes of CD for early stage ONFH.

---

* Corresponding author. Department of Orthopaedic Surgery, Stanford University School of Medicine 450 Broadway Street, Redwood City, CA, 94063, USA.
** Corresponding author. Department of Orthopedic Surgery, Stanford University School of Medicine 300 Pasteur Drive, Edwards R155, Stanford, CA, 94305, USA.
E-mail addresses: goodbone@stanford.edu (S.B. Goodman), ypyang@stanford.edu (Y.P. Yang).
[1] equally contribute

1. Introduction

Osteonecrosis of the femoral head (ONFH) is a debilitating disease that can progress to collapse, resulting in osteoarthritis of the hip. Corticosteroids, alcohol, and trauma are associated with ONFH, but the exact pathogenesis causes of ONFH remain elusive [1]. For the pre-collapse stage of ONFH, core decompression (CD) is often performed to preserve the femoral head [1,2]. However, a recent meta-analysis [3] described that an overall success rate of CD was 65%, and thus, CD does not prevent the collapse of the osteonecrotic femoral head in all cases.

Structural implants including a vascularized fibular graft (VFG), a tantalum rod, and others have been used clinically to increase mechanical strength of the osteonecrotic lesion [1]. However, the VFG has considerable donor site morbidity [4,5]. A porous tantalum metal implant has insufficient mechanical support of the subchondral bone due to little bone ingrowth into the osteonecrotic area [6].

Scaffold-based therapy has the potential to facilitate biomolecule delivery, encourage tissue ingrowth, and provide mechanical support to prevent the collapse of the femoral head due to osteonecrosis [7]. β-tri-calcium phosphate (β-TCP) has demonstrated satisfactory biocompatibility, bioresorbability, and osteoconductivity, thereby enhancing bone regeneration [8]; β-TCP-based scaffolds are rigid but typically brittle in shear and tension, and their fabrication methods can be limiting, resulting in poor quality of pore sizes [9]. In contrast, bioresorbable medical grade poly(ε-caprolactone) (PCL) is biodegradable and an FDA approved material; PCL-based scaffolds are soft but typically resistant to strain, and can be commonly used as a 3D printed material for *in vivo* applications [10]. By combining β-TCP and PCL, the resulting composite polymer takes advantage of key properties of each material to improve osteoconduction and printability of the scaffold for *in vivo* applications. Previously, we developed a novel customized, functionally-graded scaffold (FGS) [10,11] with spatially controlled porosity, degradation, and mechanical properties. The FGS is made of β-TCP and PCL and is fabricated using 3D printing [12–14]. The FGS facilitated bone ingrowth in both normal healthy rabbits [10] and rabbits with corticosteroid-associated ONFH [11].

Cell-based therapies including the injection of bone marrow derived-mononuclear cells (BM-MNCs), mesenchymal stromal cells (MSCs), and MSC-derived exosomes are also promising as biological augmentation for CD [7]. CD with BM-MNC injection (also known as bone marrow-aspirate concentrate [BMAC]) is performed clinically to regenerate the osteonecrotic lesion [1]. However, cell-based therapy does not provide mechanical support. Thus, the combination of scaffold-based and cell-based therapies for ONFH holds promise as synergistic therapies to improve the outcome of ONFH. Our previous study combining the FGS and BM-MNC injection improved bone ingrowth and decreased the number of empty lacunae in the osteonecrotic area of corticosteroid-associated ONFH [11]. It is worth noting that previous designs of the FGS were not optimized for the delivery of cells to the osteonecrotic area. For example, BM-MNCs were injected into a bone tunnel prior to FGS insertion; this has a potential risk of leakage from the bone tunnel or distribution to other locations. In addition, the effects of inserting FGS on mechanical properties of the femoral head were not confirmed.

In order to improve the outcome of CD, we designed a new porous FGS with a central channel that can facilitate the delivery of transplanted cells in a hydrogel to enhance the functionality of FGS. However, with the same dimension of the scaffold of high aspect ratio and high porosity, the addition of a relatively large central channel to the scaffold significantly increased the difficulty of 3D printing. In addition, the porous structural design (strut size, interconnected pore size, and pore geometry) of an implant such as the FGS would have important consequences on the mechanical strength and biological responses including potential for bone ingrowth, vascularization, and mineralization; these effects would be due to alterations in chemistry, biodegradation rate, and mechanical properties during implantation [15]. However, in previous studies concerning porous structural scaffolds for engineering of bone [15–17], the design and material properties of the scaffolds were variable; furthermore, the methodology of *in vivo* experiments using animal models, the implantation sites, and methods of mechanical testing have been variable. As a consequence, the optimal scaffold for the engineering of bone in ONFH is unknown. The aims of this study were two-fold: the first aim was to streamline an approach in design and fabrication to integrate any two different porous structures of the FGS; the second aim was to evaluate the efficacy of the two rationalized FGS for the treatment of corticosteroid-associated ONFH in rabbits. We fabricated two different porous structures of the FGS with 30% or 60% porosity in the segment that was within the femoral head and proximal neck using our in-house custom built 3D printer. We hypothesized that differences between FGSs with 30% and 60% porosity in the ONFH model would be significant and provide guidance and rationale for a candidate scaffold for our combinatory therapy in the future.

2. Materials and methods

2.1. Fabrication of PCL-TCP filament

Medical grade PCL (Sigma–Aldrich, St. Louis, MO, USA) pellet and β-TCP (Sigma Aldrich) powder were measured to meet the weight ratio 80/20. The 10% (wt./v) PCL and the 5% β-TCP (wt./v) solutions in N, N-Dimethylformamide (DMF, Fisher Chemical, USA) were prepared and stirred at 70 °C. After stirring for 3 h, the β-TCP solution was poured into the PCL solution, and the mixture was further stirred for an hour. The 80/20 PCL/β-TCP sheet was formed after the mixture precipitated in DI water at 20 °C, and the final product was dried for 24 h until the remaining DMF evaporated. The 80/20 PCL/β-TCP sheet was cut into small pellets (2 mm diameter) before the material was loaded into our customized filament extruder. The filament was then hot-melt extruded with a 1.1 mm-diameter nozzle at 120 °C.

2.2. Design and 3D printing of function graded scaffold

Our FGS was designed to be a hollow cylinder 32 mm in length, 3 mm in outer diameter, and 1 mm in inner diameter, with spatially graded porosity. The FGS was composed of three sections: 1-mm in length for the non-porous proximal segment, 22-mm in length for the porous (30% versus 60%) middle segment, and 9-mm in length for the 15% porous distal segment. The FGS was designed in proximal, middle, and distal segments to reflect the porosities and mechanical properties of subchondral, trabecular, and cortical bones, respectively. The porosities of proximal and distal segments were designed to be low (15%) to provide higher mechanical support to withstand the mechanical loading; the middle segment was designed to mimic the trabecular bone as the template for new bone ingrowth and vascularization. The 3D computer-aided design (CAD) model was designed in SOLIDWORKS 2018 (Dassault Systèmes SolidWorks Corporation, MA) (Fig. S1), and the finite element mesh (STL format) was exported to Slic3r to generate G-Code for the scaffolds with 15%, 30%, and 60% porosities. To implement the spatially graded porosity, two sets of G-Code (15% + 30%, and 15% + 60%) were imported to a customized Python 2.7.18 (Centrum voor Wiskunde en Informatica, Amsterdam)-based G-Code merger, which combines the G-codes based on the specified boundaries between segments (1 mm, 23 mm, 31 mm). The merged G-Code was inputted to Repetier-Host 2.1.6 (Hot-World GmbH & Co. KG, Germany), and the FGS was 3D printed by a desktop 3D printer, Lulzbot Mini 2 (Aleph Objects, Inc.), with our 80/20 PCL/β-TCP filament at 160 °C.

2.3. Analysis of FGS characterization

Three samples of each 30% or 60% porosity FGS were scanned using a microCT (Skyscan 1276, Bruker, Belgium) with 20 μm resolution at 2016 × 1344, Al 1 mm, 85 kV, 200 μA, with 2 average frames at every 0.4° angle step. NRecon software (1.6 version) was used to reconstruct data.

Reconstructed data were transferred to JPEG format and imported to a customized MATLAB program (The MathWorks, Inc., MA) for further analysis of actual porosity, pore size, and strut size. The porosity of scaffold was evaluated by

$$Porosity (\%) = \frac{V_{Total} - V_{FGS}}{V_{Total}} \times 100$$

where V_{Total} was the volume of total space covered under the scaffold, V_{FGS} was the accumulated volume of FGS over layers of microCT images. The pore size of FGS was determined by measuring the distance between struts of FGS in microCT images.

2.4. Hydrophilization and sterilization

The FGSs were hydrophilized by soaking them in 5N sodium hydroxide (NaOH, Sigma Aldrich) for 30 min after 3D printing, and the FGSs were rinsed with phosphate-buffered saline (PBS) solution and dried for 12 h. The hydrophilic scaffolds were first sterilized by soaking them in 70% ethanol for 30 min, then washing with PBS three times, then drying in the cell culture hood for 12 h, and storing them in a sterile condition until surgery.

2.5. Animal surgery

This study was approved and performed according to our institution's Animal Care and Use Committee guidelines. Eighteen male skeletally-mature New Zealand White rabbits (West Oregon Rabbit Company, OR, USA), 5–6 months of age and weighing from 4.0 to 4.5 kg, were used. The rabbits were injected with a single dose of 20 mg/kg methylprednisolone acetate (MPSL: Depo-Medrol®, Pfizer Inc, NY, USA) intramuscularly to induce corticosteroid-associated ONFH [18]. All rabbits lost approximately 10%–29% body weight, but no lethal complications were noted. Rabbits were divided into three groups (n = 6 in each group): the CD group, the 30% porosity FGS group, and the 60% porosity FGS group.

Four weeks after corticosteroid injection, surgery was performed. In brief, rabbits were anesthetized with ketamine (40 mg/kg) and xylazine (4 mg/kg) and were given buprenorphine SR (0.15 mg/kg). Additional inhalation anesthesia using isoflurane was given. In the CD group, a 20 mm skin incision was made over the proximal lateral thigh. The vastus lateralis muscle was dissected, and a small hole was made at the distal end of the third trochanter using a 2-mm-diameter round burr. Under fluoroscopic guidance, a 0.9-mm C-wire was inserted from the hole proximally towards the center of the femoral head, then a bone tunnel was made using a 3-mm-diameter cannulated drill proximally to reach 2 mm from the surface of the femoral head. The length of the bone tunnel was approximately 30 mm. In the 30% and 60% porosity FGS groups, a 30% or 60% porosity FGS was inserted into the bone tunnel after CD. The distal end of the scaffold was cut flush with bone. The wound was closed with non-absorbable suture. Antibiotics were administered for 2 days postoperatively. Two rabbits had perioperative complications: one rabbit was euthanized prior to recovery from anesthesia due to poor oxygen saturation; at necropsy, the rabbit had a pleural effusion. Another rabbit was euthanized 2 days after surgery due to urinary retention that did not resolve despite medical intervention. These two rabbits were replaced by two other rabbits. Rabbits were kept in cages and allowed free activities. At 8 weeks postoperatively, rabbits were euthanized with sodium pentobarbital, and the entire femurs were harvested.

2.6. MicroCT analysis

MicroCT scanning of femurs (six samples per group in three groups) was performed immediately after harvesting. The proximal femurs were scanned using a microCT (Skyscan 1276). The setting of microCT scanning was as same as the analysis of FGS characterization. Reconstructed data were analyzed by GEMS MicroView software (eXplore MicroView

v.2.5, Analysis Plus, GE Healthcare, Toronto, Canada).

For the area <u>inside</u> the CD in the femoral head, the total bone volume (V_{Bone}), bone ingrowth ratio, and the degradation rate of FGS were analyzed [10,11]. A 3-mm diameter X 4-mm and a 1-mm diameter X 4-mm length cylindrical regions of interest (ROIs) were co-centrically positioned at a 1-mm distance from the proximal CD or FGS site (Fig. S2A). The total volume of the ROI (V_{Total}), the total bone volume (V_{Bone}), and the remained FGS volume ($V_{Rem\ FGS}$) were measured, and the value of each item was calculated by a 3-mm diameter ROI minus a 1-mm diameter ROI. In addition, bone ingrowth ratio was calculated as the fraction of bone occupied in the available space for bone regeneration using the following formula:

$$Bone\ ingrowth\ ratio\ (\%) = \frac{V_{Bone}}{V_{Total} - V_{Rem\ FGS}} \times 100$$

The degradation rate of FGS was analyzed using following formula:

$$Degradation\ rate\ (\%) = \frac{V_{Int\ FGS} - V_{Rem\ FGS}}{V_{Int\ FGS}} \times 100$$

The initial FGS volume ($V_{Int\ FGS}$) was measured on microCT before their use.

For the area <u>outside</u> the CD in the femoral head, bone mineral density (BMD, mg/mm^3) and bone volume fraction (BVF) were evaluated. The area outside the CD was defined as the entire region of the femoral head excluding the area inside the CD. An 11-mm diameter cylindrical ROI (6-mm length) was positioned to cover the entire femoral head, and a 3-mm diameter cylindrical ROI was centrally positioned inside the CD area at the bottom of the 6-mm thickness of femoral head (Fig. S2B). BMD and BVF outside the CD were determined by calculating the data for the entire femoral head minus the data inside the CD. Thresholds were applied to differentiate between new bone and residual scaffold material in the ROI as reported previously [10,11]. A threshold value of scaffold was 45 HU and bony tissue was set 70 HU which was determined by a phantom. The specimens were stored in the −80 °C freezer after microCT scanning.

2.7. Mechanical testing

All specimens in the three groups were used. Mechanical testing was performed on a Materials Testing System fitted with a 2 KN load cell (5944 Instron Corporation, Norwood, CA) within a few days after microCT scanning. Specimens were thawed and tested at room temperature and were kept moist with PBS throughout preparation and testing. Specimens were cut 60 mm distal to the femoral head. The remaining diaphyseal bone was aligned vertically in an aluminum block and potted with polymethylmethacrylate (PMMA). PMMA was also packed under the inferior surface of the femoral neck to prevent bone deflection/fracture during testing. Indentation testing on the femoral head surface was performed in all three groups, and push-out testing on a 4 mm thick section of the femoral head was performed in the 30% and 60% porosity FGS groups. For both tests, load and displacement data were recorded at 100 Hz, and stiffness was calculated from the linear portion of load vs. displacement curve.

For indentation testing, specimens were secured in a swivel vise with the diaphyseal axis oriented 17° from vertical in the frontal plane, with the resulting load vector on the femoral head directed 17° lateral (Fig. S3A, B). This loading direction approximates the frontal plane angle at peak load during a variety of daily activities in humans [26]. Although this loading direction may not be physiologic for rabbits, it was chosen to approximate loading that would cause femoral head collapse in cases of ONFH in humans. The 1.6 mm-diameter indenter was aligned with the Ligamentum Teres in the sagittal plane and used to indent on the peak surface of the femoral head. Following the application of a 1 N compressive preload, specimens were loaded at a displacement rate of 10 mm/min until 0.5 mm displacement or 300 N to avoid a fracture at the

femoral neck.

After indentation testing, the femoral head was sectioned into two 4 mm thick segments using a 0.5 mm hand saw with a hand-made saw guide set perpendicularly along with the bone tunnel (Fig. S3C). The proximal segments in all three groups (n = 6 in each group) were used for histological analysis, whereas the middle fragments in the 30% and 60% porosity scaffold groups (n = 6 in each group) were used for push-out testing. For push-out testing, the segment of the femoral head was placed on an aluminum plate with the bone tunnel aligned above a machined recess. A 2.3 mm diameter indenter was then used to push out the scaffold vertically at the bone tunnel site and into the recess (Fig. S3D, E). Indentation tests were performed on the middle fragments in the CD group; these were indented at the bone tunnel site, as reference data for the bone tunnel after CD. A 1 N compressive preload was applied and then the specimens were loaded at 10 mm/min until failure was observed.

2.8. Histological analysis for the osteonecrotic area

The proximal fragments of specimens in all three groups (n = 6 in each group) were processed for histology. The segments were fixed in 4% paraformaldehyde (pH 7.4) and decalcified in 0.5M ethyl-enediaminetetraacetic acid (EDTA; pH 7.4). The segments were embedded in optimal cutting temperature compound, and an 8-μm longitudinal frozen section parallel to the direction of the drill hole/femoral neck axis was obtained. Sections were stained with hematoxylin and eosin (H&E) and examined under a microscope (BZ-X 710 digital microscope: Keyence, Osaka, Japan). In addition, as previously reported [19], woven bone tissue was assessed using GFP fluorescent light (green filter: 450–490 nm wavelength), and BVF inside the drill hole was evaluated histologically using ImageJ. For the area outside the bone tunnel, a total of five fields in the subchondral area of the femoral head were randomly selected under 200× magnification. The femoral head was determined to demonstrate histological signs of osteonecrosis when the following two findings were present: 1) empty lacunae and pyknotic nuclei of osteocytes within the subchondral bone, 2) bone marrow cell necrosis, fatty bone marrow without hematopoietic cells, scant bone marrow, or reparative tissue such as accumulating multinuclear cells, granulation tissue, fibrosis, or appositional bone formation with osteoblast-like cells around the osteonecrotic lesion within the region of bone marrow [18,20]. In addition, to accurately assess the breadth of the osteonecrotic changes, the total cell numbers, and the number of empty lacunae in the trabecular bone were manually and blindly counted by two investigators individually; the percentage of empty lacunae was calculated. The repair pattern of the bone marrow was evaluated by two investigators, based on the following findings: percentage of appositional bone formation area in the total area of reparative tissues; reparative osteogenesis (>60%); unclassified (40%–60%); destructive repair (<40%) [21,22].

2.9. Statistical analysis

Student's *t*-test was performed for parametric data with two groups. A one-way ANOVA with Tukey's multiple comparisons test and the Kruskal–Wallis test with Dunn's multiple comparisons test were performed for parametric and nonparametric data with three groups, respectively. The internal reliability of the percentage of empty lacunae between two investigators was assessed by intraclass correlation coefficients (ICC). All data were reported as mean ± standard deviation. A value of $p < 0.05$ was chosen as statistical significance. Based on previous data [11], a sample size of six per group was set by power analysis with $\alpha = 0.05$ and $\beta = 0.20$ to detect significant differences between the groups using analysis of *t*-tests.

3. Results

3.1. FGS characterization

Photographs of the FGS are shown in Fig. 1. The actual porosity of the middle segment of "30%" and "60%" porosity FGSs was 26.4% ± 2.3% and 56.0% ± 4.5%, respectively. The pore size of the 30% porosity FGS was 699 ± 56 μm, whereas the pore size of the 60% one was 999 ± 71 μm, which was significantly larger than the pores in the 30% porosity FGS ($p < 0.001$). Actual strut sizes of the middle segments of 30% and 60% porosity FGS were 324 ± 60 μm and 351 ± 38 μm; there was no significant difference between the two groups ($p = 0.55$). In addition, the actual porosity, pore size, and strut size of the distal segment of FGS were 10.6% ± 1.1%, 228 ± 31 μm, and 294 ± 43 μm, respectively.

3.2. The 30% porosity FGS accelerated bone ingrowth inside the CD area on microCT

The results of microCT analysis are shown in Fig. 2. Mineralized tissue was noted inside the drill hole in the CD group. In both the 30% and 60% porosity FGS groups, mineralized tissue was also confirmed inside the FGS. The total bone volume was 10.0 ± 3.3 mm^3 in the CD group, which was significantly higher than in both the 30% porosity FGS group (6.0 ± 1.6 mm^3, $p < 0.05$) and the 60% porosity FGS group (5.4 ± 2.7 mm^3, $p < 0.05$). There were no differences between the 30% and 60% porosity FGS groups. However, the bone ingrowth ratio was 39.5 ± 13.0% in the CD group, 73.9 ± 15.8% in the 30% porosity FGS group, and 61.3 ± 30.1% in the 60% porosity FGS group. Bone ingrowth ratio in the 30% porosity FGS group was significantly higher than in the CD group ($p < 0.05$). The 60% porosity FGS group had no significant differences in bone ingrowth compared to the CD group or the 30% porosity FGS group. The degradation rate of FGS was 19% ± 8% in the 30% porosity FGS and 26% ± 11% in the 60% porosity FGS; there was no significant difference in degradation rate ($p = 0.21$).

There were no significant differences in BMD or BVF in the area outside the CD among the three groups.
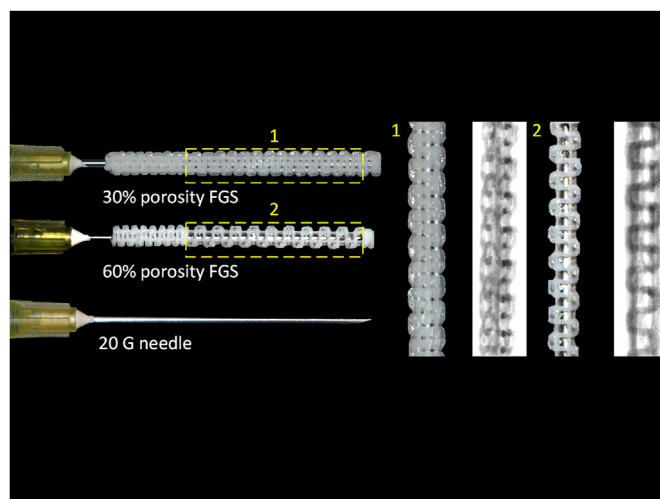
Fig. 1. Macrographs and microCT images of the 30% and 60% porosity FGSs. The FGS was a hollow cylinder 32 mm in length, 3 mm in outer diameter, and 1 mm in inner diameter, with spatially graded porosity. The FGS was split into three sections: 1 mm in length for the filled proximal segment, 22 mm in length for the porous (30% and 60%) middle segment, and 9 mm in length for the less porous (15%) distal segment.
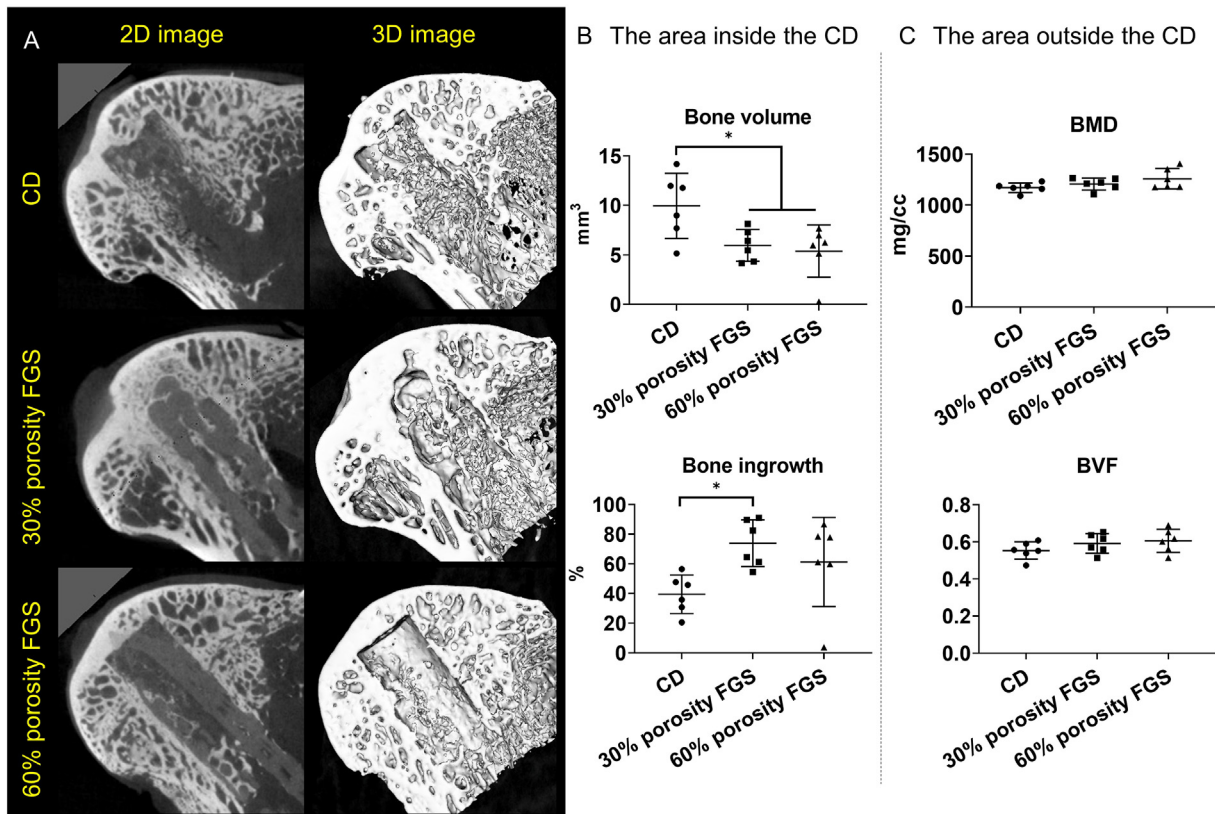
Fig. 2. Representative microCT reconstructed images and analysis results (A) Mineralized tissue was noted in the CD group. In both the 30% and 60% porosity FGS groups, mineralized tissue was confirmed inside the FGS (B) The area inside the CD. Bone volumes in the CD group were significantly higher than in both FGGs groups. While bone ingrowth ratio in the 30% porosity FGS group was significantly higher than in the CD group (*$p < 0.05$ by Tukey's multiple comparisons test) (C) The area outside the CD. No differences in BMD and BVF were found among the three groups.

3.3. The 30% porosity FGS group showed superior biomechanical properties inside the CD area

The push-out test demonstrated that the stiffness at the bone tunnel in the 30% porosity FGS group was significantly higher compared to the 60% porosity FGS group (582.4 $\pm$ 192.3 N/mm^3 in the 30% porosity FGS group, and 338.7 $\pm$ 164.6 N/mm^3 in the 60% porosity FGS group, $p <$ 0.05). The indentation test showed that the stiffness at the bone tunnel in the CD group was 552.1 $\pm$ 304.2 N/mm^3.

The indentation test showed no difference in stiffness at the femoral head surface among the three groups (752.3 $\pm$ 89.1 N/mm^3 in the CD group, 732.2 $\pm$ 118.2 N/mm^3 in the 30% porosity FGS group, and 802.8 $\pm$ 139.9 N/mm^3 in the 60% porosity FGS group) (Fig. 3).

*p < 0.05 by *t*-test
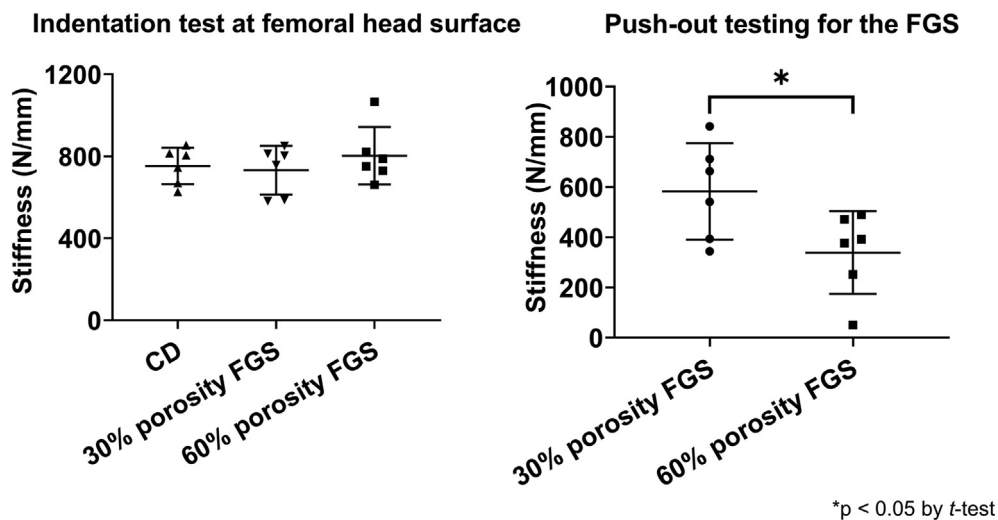
Fig. 3. Mechanical testing results (A) The indentation testing for the surface of the femoral head. No difference in stiffness was found among the three groups (B) The push-out testing for FGS in the middle segment. The stiffness in the 30% porosity FGS group was significantly higher compared to the 60% porosity FGS group (*$p <$ 0.05 by Student's t-test).

3.4. Histological analysis of the femoral head after CD with/without the FGS

Representative images of H&E staining and GFP fluorescent images of the femoral head are shown in Fig. 4 and Fig. 5, respectively. Spicules of trabecular bone were seen in the area inside the drill hole in the CD group. In the 30% porosity FGS group, thick and mature trabecular bone was noted around the porous FGS. In contrast, in the 60% porosity FGS group, thinner, more immature trabecular bone was noted around the porous FGS. BVF inside the drill hole was 0.23 ± 0.14 in the CD group, 0.38 ± 0.16 in the 30% porosity FGS, and 0.16 ± 0.13 in the 60% porosity FGS. BVF inside the drill hole in the 30% porosity FGS group was significantly higher than in the 60% porosity FGS group ($p < 0.05$). The CD group showed no significant differences in BVF inside the drill hole compared to the FGS groups of 30% and 60% porosity. The majority of fields in the region of the subchondral bone in all the three groups demonstrated scant bone marrow with neither adipocytes nor hematopoietic cells; this was often accompanied by reparative tissues such as accumulating multinuclear cells, granulation, and fibrous tissues: however, little sign of appositional bone formation with osteoblast-like cells around the osteonecrotic lesion was seen. Osteocytes with pyknotic nuclei were commonly seen in the trabecular bone. Based on the above criteria, all femoral heads were diagnosed as demonstrating evidence of early osteonecrosis with destructive repair (Fig. 6). The ICC for the two investigators counting the percentage of empty lacunae was $r = 0.922$ (95% CI: 0.94 to 0.98, $p < 0.0001$). The percentage of empty lacunae was $50.8\% \pm 10.3\%$ in the CD group, $53.9\% \pm 14.1\%$ in the 30% porosity FGS group, and $51.9\% \pm 14.9\%$ in the 60% porosity FGS group (no difference).

4. Discussion

Although numerous scaffolds have been reported for use in ONFH [7], to our knowledge, no scaffold has been designed for both mechanical support and use with cell-based therapy for augmentation of CD, except for our prior study [11]. However, previous designs of the FGS were not optimized for the delivery of cells to the osteonecrotic area. Our new design of the FGS to fill the CD region of the osteonecrotic femoral head has spatially controlled porosity with a central channel to accommodate different opportunities for treatment. In this study, we demonstrated that the central channel of FGS can accommodate a surgical needle (gauge 18, OD 0.9–1 mm), and the channel structure remains intact after the retraction of the surgical needle. Our next study is to examine if there are added benefits in osteonecrosis of the hip by the combination of this centrally channeled scaffold with a biological laden injectable hydrogel, which was recently developed by our group [23]. Due to its established biocompatibility, biodegradability, and extrudability, the composite of PCL and β-TCP with an 80/20 ratio was used as the 3D printing material for the FGS. The mechanical and degradation properties of 80/20 PCL/β-TCP scaffolds have been previously reported [10]. The apparent
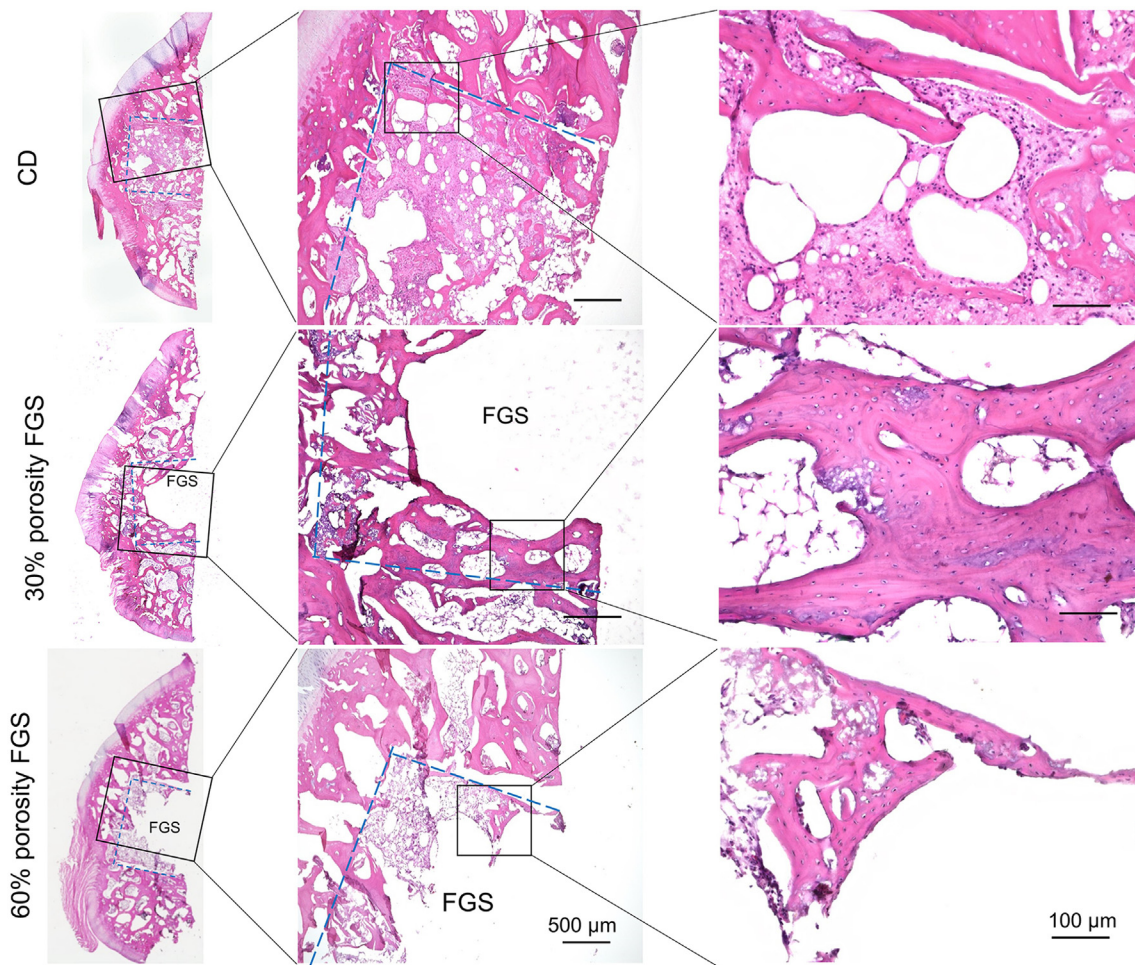
Fig. 4. Representative H&E staining photomicrographs of the femoral head. H&E staining (Magnification: 40x and 200x) showed that trabecular bones in the area inside CD were seen in the CD group. In the 30% porosity FGS group, thick trabecular bones were noted around the porous FGS. In contrast, in the 60% porosity FGS group, trabecular bones around the porous FGS were thin, and newly immature bones were confirmed. The empty spaces inside the bone tunnel in the FGS groups are artifacts left behind by scaffold struts detached during the staining process. Blue dash line: the area inside the CD.
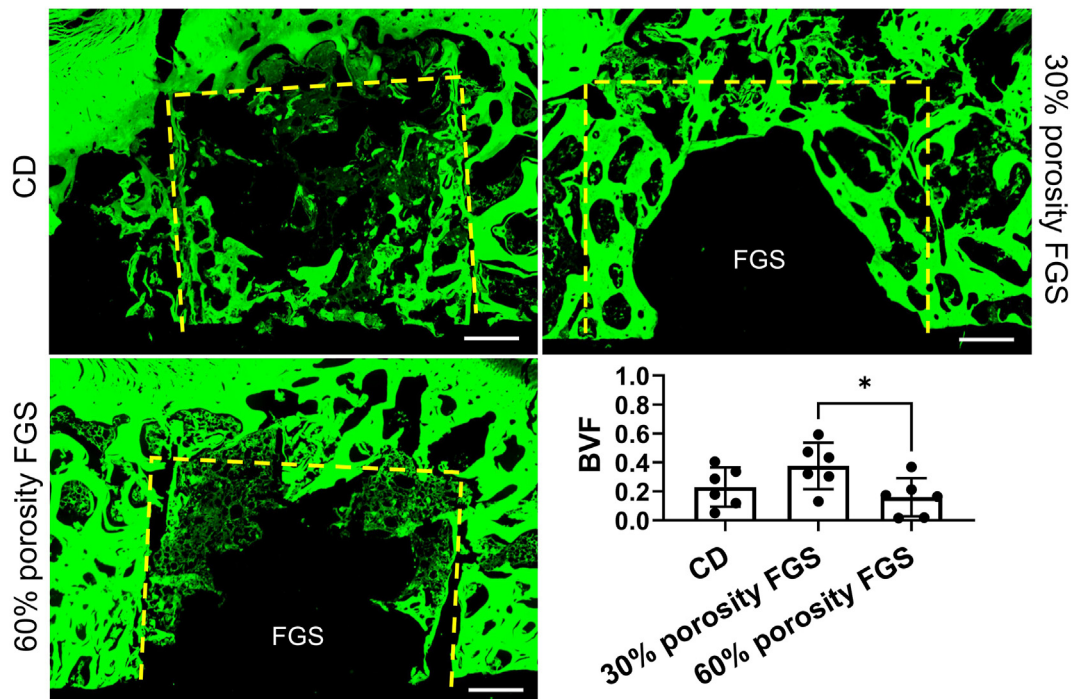
Fig. 5. Representative fluorescent images of H&E staining photomicrographs of the femoral head. fluorescent images of H&E staining (Magnification: 40x) in the 30% porosity FGS group showed that thick trabecular bones were noted around the porous FGS. In contrast, in the 60% porosity FGS group, less and thin trabecular bones around the porous FGS were confirmed. BVF inside drill hole in the 30% porosity FGS was significantly higher than in the 60% porosity FGS (*p < 0.05). The empty spaces inside the bone tunnel in the FGS groups are artifacts left behind by scaffold struts detached during the staining process. Yellow dash line: the area inside the CD.

moduli of 60%–15% FGSs ranged from 51.5 to 213.4 MPa. The degradation rates of the macroporous 80/20 PCL/β-TCP scaffolds at 8 weeks after implantation in the femoral head were approximately 26% in normal healthy rabbits [10] and approximately 19% in the rabbits with corticosteroid-associated ONFH [11]. Our 24-week subcutaneous implantation study showed the degradation rate of 80/20 PCL/β-TCP filaments was 7% [24]. In this study, we adapted the materials and the design of the FGS such that the porosity was approximately 30% or 60%, to verify the effect of porosity on bone ingrowth and vascularization.

MicroCT analysis showed that the 30% porosity FGS promoted bone ingrowth compared to CD only. It is worth noting that both the 30% and 60% porosity FGS groups had lower total bone volume compared to the CD group. This is probably due to the fact that FGS occupied space in the bone tunnel; consequently, the available space for bone regeneration was limited. In contrast, the bone ingrowth ratio in the 30% porosity FGS group was higher compared to the CD group, which indicated that the 30% porosity FGS accelerated bone bridging and osseointegration and contributed to improved mechanical properties. In the push-out test, the 30% porosity FGS (approximately 600 N/mm^2) was also biomechanically superior compared to the 60% porosity FGS (approximately 350 N/mm^2) in the CD area. Based on our previous studies [10,14], the stiffness of the previous design of FGS itself was approximately 100 N/mm^2 in the 30% porosity segments and approximately 50 N/mm^2 in the 60% porosity segment. On the other hand, the new FGS that was used in this study adopted a similar design to the previous FGS and used the same materials; the differences were the addition of a central channel which may decrease the mechanical properties of the scaffolds. In addition, both FGSs degraded approximately 20%–25% at 8 weeks after surgery. Thus, these findings indicated that the main contributor of push-out strength may be the combination of bone ingrowth and frictional force due to contact surface area between the FGSs and surrounding bone, not FGSs themselves. Furthermore, FGSs were press-fit in the bone tunnel, and the 30% porosity FGS had higher contact surface area and generated more frictional force compared to the 60% porosity FGS, which may be one of

the reasons that the 30% porosity FGS provided a higher mechanical push-out strength. The stiffness at the bone tunnel in the CD group was approximately 550 N/mm^2; this biomechanical property of the bone tunnel in the 30% porosity FGS was close to the CD group. It is worth noting that although 30% porosity FGS had lower bone volume at the bone tunnel, the FGS could provide similar mechanical strength as CD only.

Histological analysis revealed that thick trabeculae of bone were present around the 30% porosity FGS, and the BVF inside the drill hole in the 30% porosity FGS group was significantly higher compared to the 60% porosity FGS group. The approximate pore size was 700 μm in the 30% porosity FGS and 1000 μm in the 60% porosity FGS. Taniguchi et al. [25] implanted three different pore sizes (the P300, P600, and P900 implants with a mean pore size of 309, 632, and 956 μm, respectively) of titanium implants with 65% porosity into the cancellous bone of femurs in rabbits; the P600 implant demonstrated superior fixation than the other two implants, and the P300 implant had lower bone ingrowth. Ran et al. [26] inserted three different pore sizes (400 μm, 600 μm, 800 μm) of porous cylindrical titanium-based scaffolds into the bone tunnel in the distal femoral condyle in rabbits. The scaffold with a pore size of 600 μm showed superior bone ingrowth, maturation of bone formation, and bone-implant fixation stability compared to the other scaffolds. The scaffold with a pore size of 400 μm had thick but sparse trabecular bone, whereas trabecular bone in the scaffold with a pore size of 800 μm was thinner and less mature. Despite different materials for the scaffolds, the results using porous titanium are similar to our results using a composite scaffold.

We fabricated the FGS using a quadrangular pore geometry. Rotbaum et al. [27] demonstrated that the mechanical properties of PCL scaffolds strongly depend on the pore size (larger pore sizes decreased the mechanical strength) rather than pore geometry. Thus, these results indicate that the pore size affected new bone formation to a greater degree than pore geometry in our study; this suggests that the 60% porosity FGS with a pore size of approximal 1000 μm would require a time period greater
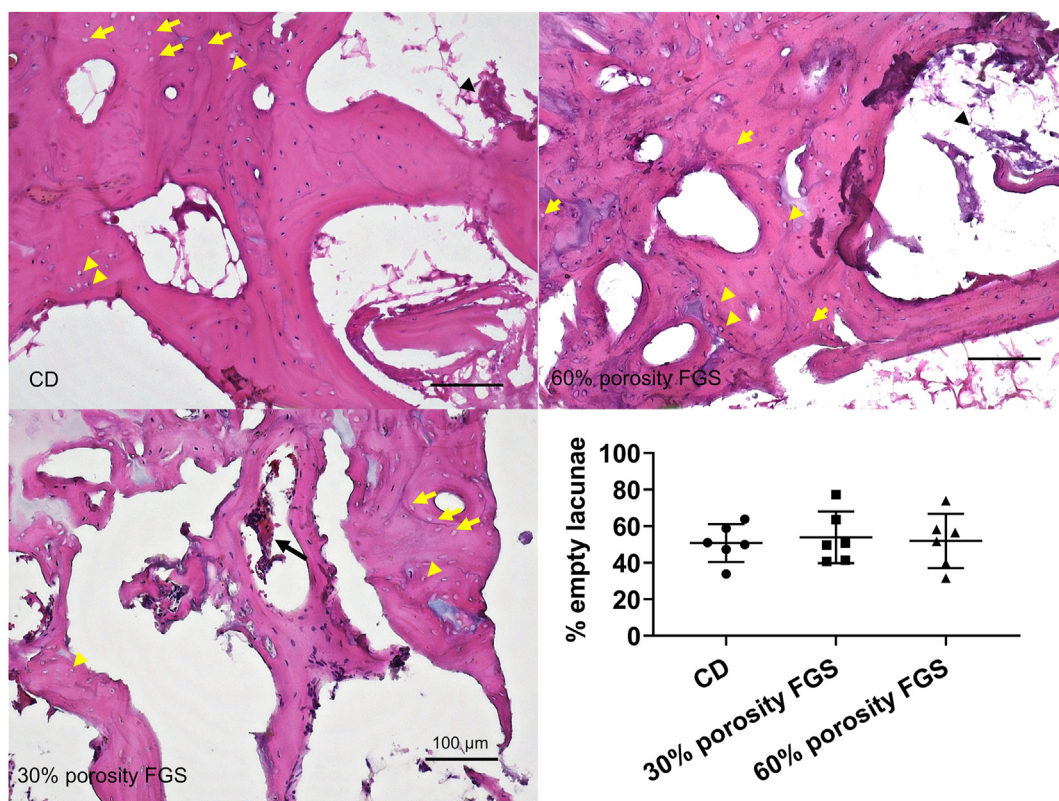
Fig. 6. H&E staining photomicrographs of the area outside the CD and the percentage of empty lacunae. H&E staining (magnification: 200x) in the region of the subchondral bone. The majority of fields in the region of the subchondral bone in all the three groups demonstrated scant bone marrow with neither adipocytes nor hematopoietic cells, often accompanied by reparative tissues such as accumulating multinuclear cells (black arrow), granulation, and fibrous tissues (black arrowhead); little sign of appositional bone formation with osteoblast-like cells around the osteonecrotic lesion was seen. In addition, a large number of empty lacunae (yellow arrow) were noted and pyknotic nuclei of osteocytes with peripherally displaced nuclei (yellow arrowhead) were seen in the trabecular bone. The percentage of empty lacunae was no significant difference among the three groups.

than 8 weeks to form mature bone tissue. Therefore, the 30% porosity FGS with a pore size of approximately 700 μm seems optimal to enhance bone regeneration and improve the mechanical properties of the bone tunnel after CD in the osteonecrotic area of the femoral head.

In this study, the porosity of the scaffold was assigned to Slic3r, an open-source program for 3D printing G-codes, and the pore size was calculated and determined based on the porosity. The porosity and pore size of the scaffold were coupled; both parameters were determined and changed simultaneously. Hence fixing one parameter while tuning another was not achievable.

As expected, both 30% and 60% porosity FGSs did not negatively impact BMD, BVF, and the number of empty lacunae outside the CD and the mechanical properties of the femoral head surface due to the intact cortical shell and evaluation time window at 8 weeks after treatment. However, the new porous FGS with a central channel is designed to be combined with cell-based therapy. In addition, a previous study [28] demonstrated that the stiffness of cancellous bone of the femoral head was 900 (389–2248) MPa in healthy humans with a mean age of 45 years. This result and our results are not directly comparable, but suggests that the biomechanical properties at the bone tunnel in the 30% FGS group may be not optimized. Further studies are needed to reveal the efficacy of the combination of scaffold-based and cell-based therapies for ONFH.

A previous study [29] demonstrated that freeze–thaw cycles of up to eight times did not affect the biomechanical or morphologic properties of fibular allograft segments. In our study, all samples were processed for mechanical testing after a single freeze–thaw cycle. In addition, all precautions have been taken into consideration to minimize any potential effects on the results of mechanical testing.

There are several limitations in this study. First, we used a model of corticosteroid-associated ONFH in rabbits to simulate early stage ONFH in humans. Although there are several protocols to develop a rabbit model of corticosteroid-associated ONFH including corticosteroids only, corticosteroids plus lipopolysaccharide (LPS) or allogenic serum, the ideal animal model has not yet been established [30]. The protocol with multiple injections of MPSL plus LPS has been reported to induce osteonecrotic lesions in a percentage as high as 93% at 2–6 weeks [31–33]. Initially, we tried this protocol, but the mortality rate was high due to serious loss of body weight and respiratory tract infection. Alternatively, the single injection of MPSL has been reported to induce osteonecrotic lesions in a percentage as high as 80% at 4 weeks [18,34, 35]. However, in an ongoing series of experiments in which both male and female rabbits were used, we found that the mortality rate in female rabbits (25%) was substantially higher than in males (8%) [38]. Based on these findings, we used male rabbits only in this study. Two rabbits in our series had to be euthanized due to complications: one rabbit's death was associated with a pleural effusion that might be related to MPSL injection; the other animal's urinary retention was probably unrelated. The actual mortality rate due to MPSL injection in the present study was 5% (one of 20 male rabbits). Thus, we believe that the model used in the current study is well-established and is one of the safest, clinically relevant models currently available for rabbits [11]. Second, several definitions for identifying the histopathology of ONFH have been reported [18, 36]; however, complete consensus is not yet established [37]. Kawai et al. [20] demonstrated that healthy rabbits without any corticosteroid treatment had bone marrow containing hematopoietic cells; the majority of the osteocytes had round or oval nuclei but empty lacunae were rarely seen. Conversely, corticosteroid-treated rabbits had bone marrow

replaced by enlarged fat cells without hematopoietic cells, and pyknosis of osteocytes with peripherally displaced nuclei which were concentrated within the subchondral bone. Yamamoto et al. [18] reported that in 25% of the femurs, necrotic bone marrow was almost wholly replaced by reparative tissue such as granulation tissue, fibrosis, or appositional bone formation at 10 weeks after corticosteroid injection in rabbits. The endpoint in our study was 12 weeks after MPSL injection (8 weeks after surgery). Thus, based on these findings, we diagnosed femoral head osteonecrosis histologically when the following two findings were present: 1) empty lacunae and pyknotic nuclei of osteocytes within the region of subchondral bone, 2) bone marrow cell necrosis, fatty bone marrow without hematopoietic cells, scant bone marrow, or reparative tissue such as granulation tissue, fibrosis, or appositional bone formation with osteoblast-like cells around the osteonecrotic lesion within the region of bone marrow. In addition, the repair pattern of bone marrow was evaluated, based on the percentage of appositional bone formation area in the total area of reparative tissues [21,22]. All the femoral heads had the two important histological findings and were diagnosed as showing early ONFH with destructive repair. Third, the FGS is degraded by heat and xylene during paraffin-embedding. To avoid this situation, frozen sections were used for specimen processing. However, during the sectioning process, FGSs would occasionally curl and peel off from the glass plate, so that the FGS itself could not be directly evaluated in the histological analysis. As a consequence, some new bone formed inside and around the FGS might have been detached and washed out during processing and staining.

In conclusion, we designed a new porous FGS, using PCL/β-TCP fabricated by a 3D printer, containing a central channel to be used with cell-based therapy. We compared two different FGSs of 30% or 60% porosity, with respect to bone regeneration and mechanical properties in the bone tunnel at 8 weeks after CD. The 30% porosity FGS promoted bone ingrowth and resulted in superior biomechanical properties within the bone tunnel. This FGS implant may be useful in improving the outcomes of CD for early stage ONFH.

Declaration of competing interest

The author(s) have no conflicts of interest relevant to this article.

Appendix A. Supplementary data

Supplementary data to this article can be found online at https://doi.org/10.1016/j.jot.2021.01.002.

References

[1] Mont MA, Salem HS, Piuzzi NS, Goodman SB, Jones LC. Nontraumatic osteonecrosis of the femoral head: where do we stand today?: a 5-year update. J Bone Joint Surg Am 2020;102(12):1084–99.

[2] Chughtai M, Piuzzi NS, Khlopas A, Jones LC, Goodman SB, Mont MA. An evidence-based guide to the treatment of osteonecrosis of the femoral head. Bone Joint Lett J 2017;99-B(10):1267–79.

[3] Hua KC, Yang XG, Feng JT, Wang F, Yang L, Zhang H, et al. The efficacy and safety of core decompression for the treatment of femoral head necrosis: a systematic review and meta-analysis. J Orthop Surg Res 2019;14(1):306.

[4] Cao L, Guo C, Chen J, Chen Z, Yan Z. Free vascularized fibular grafting improves vascularity compared with core decompression in femoral head osteonecrosis: a randomized clinical trial. Clin Orthop Relat Res 2017;475(9):2230–40.

[5] Moya-Angeler J, Gianakos AL, Villa JC, Ni A, Lane JM. Current concepts on osteonecrosis of the femoral head. World J Orthoped 2015;6(8):590–601.

[6] Tanzer M, Bobyn JD, Krygier JJ, Karabasz D. Histopathologic retrieval analysis of clinically failed porous tantalum osteonecrosis implants. J Bone Joint Surg Am 2008;90(6):1282–9.

[7] Maruyama M, Lin T, Pan CC, Moeinzadeh S, Takagi M, Yang YP, et al. Cell-based and scaffold-based therapies for joint preservation in early-stage osteonecrosis of the femoral head: a review of basic research. JBJS Rev 2019;7(9):e5.

[8] Samavedi S, Whittington AR, Goldstein AS. Calcium phosphate ceramics in bone tissue engineering: a review of properties and their influence on cell behavior. Acta Biomater 2013;9(9):8037–45.

[9] Diao J, OuYang J, Deng T, Liu X, Feng Y, Zhao N, et al. 3D-Plotted beta-tricalcium phosphate scaffolds with smaller pore sizes improve in vivo bone regeneration and biomechanical properties in a critical-sized calvarial defect rat model. Adv Healthc Mater 2018;7(17). e1800441.

[10] Kawai T, Shanjani Y, Fazeli S, Behn AW, Okuzu Y, Goodman SB, et al. Customized, degradable, functionally graded scaffold for potential treatment of early stage osteonecrosis of the femoral head. J Orthop Res 2018;36(3):1002–11.

[11] Maruyama M, Nabeshima A, Pan CC, Behn AW, Thio T, Lin T, et al. The effects of a functionally-graded scaffold and bone marrow-derived mononuclear cells on steroid-induced femoral head osteonecrosis. Biomaterials 2018;187:39–46.

[12] Shanjani Y, Pan CC, Elomaa L, Yang Y. A novel bioprinting method and system for forming hybrid tissue engineering constructs. Biofabrication 2015;7(4):045008.

[13] Shanjani Y, Kang Y, Zarnescu L, Ellerbee Bowden AK, Koh JT, Ker DFE, et al. Endothelial pattern formation in hybrid constructs of additive manufactured porous rigid scaffolds and cell-laden hydrogels for orthopedic applications. J Mech Behav Biomed Mater 2017;65:356–72.

[14] Bruyas A, Lou F, Stahl AM, Gardner M, Maloney W, Goodman S, et al. Systematic characterization of 3D-printed PCL/beta-TCP scaffolds for biomedical devices and bone tissue engineering: influence of composition and porosity. J Mater Res 2018; 33(14):1948–59.

[15] Zhang L, Yang G, Johnson BN, Jia X. Three-dimensional (3D) printed scaffold and material selection for bone repair. Acta Biomater 2019;84:16–33.

[16] Perez RA, Mestres G. Role of pore size and morphology in musculo-skeletal tissue regeneration. Mater Sci Eng C Mater Biol Appl 2016;61:922–39.

[17] Dwivedi R, Kumar S, Pandey R, Mahajan A, Nandana D, Katti DS, et al. Polycaprolactone as biomaterial for bone scaffolds: review of literature. J Oral Biol Craniofac Res 2020;10(1):381–8.

[18] Yamamoto T, Irisa T, Sugioka Y, Sueishi K. Effects of pulse methylprednisolone on bone and marrow tissues: corticosteroid-induced osteonecrosis in rabbits. Arthritis Rheum 1997;40(11):2055–64.

[19] Ren PG, Ma T, Huang Z, Smith RL, Goodman SB. Quantitation of bone area in undecalcified frozen sections with fluorescent microscopy. J Histotechnol 2008; 38(1):15–7.

[20] Kawai K, Tamaki A, Hirohata K. Steroid-induced accumulation of lipid in the osteocytes of the rabbit femoral head. A histochemical and electron microscopic study. J Bone Joint Surg Am 1985;67(5):755–63.

[21] Zhang G, Sheng H, He YX, Xie XH, Wang YX, Lee KM, et al. Continuous occurrence of both insufficient neovascularization and elevated vascular permeability in rabbit proximal femur during inadequate repair of steroid-associated osteonecrotic lesions. Arthritis Rheum 2009;60(10):2966–77.

[22] Zheng LZ, Cao HJ, Chen SH, Tang T, Fu WM, Huang L, et al. Blockage of src by specific siRNA as a novel therapeutic strategy to prevent destructive repair in steroid-associated osteonecrosis in rabbits. J Bone Miner Res 2015;30(11):2044–57.

[23] Moeinzadeh S, Park Y, Lin S, Yang YP. In-situ stable injectable collagen-based hydrogels for cell and growth factor delivery. Materialia (Oxf) 2021;15:100954.

[24] Kang JH, Kaneda J, Jang JG, Sakthiabirami K, Lui E, Kim C, et al. The influence of electron beam sterilization on in vivo degradation of beta-TCP/PCL of different composite ratios for bone tissue engineering. Micromachines 2020;11(3).

[25] Taniguchi N, Fujibayashi S, Takemoto M, Sasaki K, Otsuki B, Nakamura T, et al. Effect of pore size on bone ingrowth into porous titanium implants fabricated by additive manufacturing: an in vivo experiment. Mater Sci Eng C Mater Biol Appl 2016;59:690–701.

[26] Ran Q, Yang W, Hu Y, Shen X, Yu Y, Xiang Y, et al. Osteogenesis of 3D printed porous Ti6Al4V implants with different pore sizes. J Mech Behav Biomed Mater 2018;84:1–11.

[27] Rotbaum Y, Puiu C, Rittel D, Domingos M. Quasi-static and dynamic in vitro mechanical response of 3D printed scaffolds with tailored pore size and architectures. Mater Sci Eng C Mater Biol Appl 2019;96:176–82.

[28] Martens MVAR, Delport P, De Meester P, Mulier JC. The mechanical characteristics of cancellous bone at the upper femoral region. J Biomech 1983;16(12):971–83.

[29] Shaw JM, Hunter SA, Gayton JC, Boivin GP, Prayson MJ. Repeated freeze-thaw cycles do not alter the biomechanical properties of fibular allograft bone. Clin Orthop Relat Res 2012;470(3):937–43.

[30] Xu J, Gong H, Lu S, Deasey MJ, Cui Q. Animal models of steroid-induced osteonecrosis of the femoral head-a comprehensive research review up to 2018. Int Orthop 2018;42(7):1729–37.

[31] Sheng H, Zhang G, Wang YX, Yeung DK, Griffith JF, Leung KS, et al. Functional perfusion MRI predicts later occurrence of steroid-associated osteonecrosis: an experimental study in rabbits. J Orthop Res 2009;27(6):742–7.

[32] Xie XH, Wang XL, Yang HL, Zhao DW, Qin L. Steroid-associated osteonecrosis: epidemiology, pathophysiology, animal model, prevention, and potential treatments (an overview). J Orthop Translat 2015;3(2):58–70.

[33] Qin L, Zhang G, Sheng H, Yeung KW, Yeung HY, Chan CW, et al. Multiple bioimaging modalities in evaluation of an experimental osteonecrosis induced by a combination of lipopolysaccharide and methylprednisolone. Bone 2006;39(4): 863–71.

[34] Motomura G, Yamamoto T, Miyanishi K, Kondo K, Hirota Y, Iwamoto Y. Risk factors for developing osteonecrosis after prophylaxis in steroid-treated rabbits. J Rheumatol 2008;35(12):2391–4.

[35] Miyanishi K, Yamamoto T, Irisa T, Yamashita A, Motomura G, Jingushi S, et al. Effects of cyclosporin A on the development of osteonecrosis in rabbits. Acta Orthop 2006;77(5):813–9.

[36] Zhu H, Cai X, Lin T, Shi Z, Yan S. Low-intensity pulsed ultrasound enhances bone repair in a rabbit model of steroid-associated osteonecrosis. Clin Orthop Relat Res 2015;473(5):1830–9.

[37] Parajuli S, Fowler JR, Balasubramanian E, Reinus WR, Gaughan JP, Rosenthal DI, et al. Problems with the pathological diagnosis of osteonecrosis. Skeletal Radiol 2016;45(1):13–7.

[38] Maruyama M, Lin T, Kaminow NI, Thio T, Storaci HW, Pan CC, et al. The efficacy of core decompression for steroid-associated osteonecrosis of the femoral head in rabbits. J Orthop Res 2020 Oct 23. Epub ahead of print.